UNIVERSITY OF MILANO-BICOCCA

ESA LIVING PLANET FELLOWSHIP 2018

FINAL REPORT

MULTI-FLEX: towards a strategy for fluorescence monitoring at multiple scales within the context of the FLEX/S-3 tandem mission

Author
Dr Marco Celesti

2nd December 2020

Contents

1 Executive summary

This report covers the two years of activity of the Living Planet Fellowship project "MULTI-FLEX" (ESA/Contract No. 4000125442/18/I-NS). The current status of the activity for the different Work Packages (WPs) is reported in Table 1. The main development of the retrieval routine for fluorescence and vegetation parameters from FLOX time series (WP1) was completed. At the same time, the convolution of FLOX data to the S-3 OLCI "FLEX mode" spectral response functions was performed (WP2). A thorough evaluation of the feasibility of fluorescence retrieval in the O_2-A and O_2-B band was performed. Surface fluorescence/reflectance data collected with the HyPlant sensor were convolved to the Sentinel-2 and to the Sentinel-3B "FLEX mode" spatial and spectral resolution (WP3). Different sampling strategies to characterize the spatial representativeness of fluorescence at the FLEX pixel spatial scale were evaluated, together with the identification of Sentinel-2 based proxies for tracking fluorescence heterogeneity. A full atmospheric correction of the Sentinel-3B "FLEX mode" data was not performed, nevertheless a proof-of-concept for a bottom-up approach from HyPlant airborne data is presented (WP4). Due to

the fact that Level-1b (L-1b) data from the "FLEX mode" S-3B OLCI were not available at the beginning of the project, an additional WP (WP5) was put in place to cover the processing of the "FLEX mode" S-3B OLCI from L-0 to L-1b. This was achieved following a 6-months stay at ESA-ESTEC in Noordkwijk (The Netherlands) from 1st February 2019 to 31st July 2019.

WP	Description	Status at mid term
WP1	Development of a processing chain for coupled retrieval of fluorescence and vegetation parameters from continuous ground hyperspectral measurements	Completed
WP2	Adaptation of the inversion scheme to the spectral resolution of the reconfigured Sentinel-3B OLCI	Completed for radiance based retrievals; RTM inversion did not succeed
WP3	Exploiting HyPlant and Sentinel-3A TOC products to test simple fluorescence-derived metrics	Completed with addition of cal/val sampling
WP4	Scaling of the scheme proposed in WP2 to the reconfigured OLCI-B TOC data	Not applicable to TOA radiance; proof-of-concept provided with bottom-up approach
WP5	Processing of the reconfigured Sentinel-3B OLCI data to L1b TOA radiances	Added to the original proposal with a CCN; Completed

Table 1: Summary of the status of the different Work Packages (WPs) of the project.

2 Objectives and workplan

2.1 Scientific context

Terrestrial vegetation plays a critical role in the global biogeochemical cycles (Franklin et al., 2016), and as any other element in the Earth-surface system, its energy budget is strongly driven by solar radiation through a complex system of processes (*e.g.*, Monson and Baldocchi 2013). From a physiological point of view, the key process that originates from this interaction is photosynthesis. Hyperspectral Remote Sensing (RS) data have been exploited in the last decades to successfully retrieve information at different scales about plant properties strongly linked with the photosynthetic process. The inherent strength of RS techniques for monitoring terrestrial ecosystems resides in their ability to cope with processes that are highly dynamic, both spatially and

temporally at a relevant scale for describing them. In the last years, RS of solar-induced chlorophyll fluorescence (SIF) emerged as a novel and promising scientific field for studying the dynamic behavior of photosynthesis (for a review see Meroni et al. 2009; Mohammed et al. 2019; Porcar-Castell et al. 2014). SIF is a physical side product of chlorophyll a light absorption that is emitted as an electromagnetic radiation in the red and far-red spectral regions ($\approx$ 650–850 nm), and it is related to the energetic status of the photosystems. Nevertheless, apart from physiology SIF is concurrently influenced by leaf and canopy structure, pigment concentration and weather\illumination conditions, and its unambiguous interpretation is still challenging. All these parameters change in space and time, and their variability must be considered towards an unbiased interpretation of the SIF signal.

The FLuorescence EXplorer (FLEX), selected as the 8th ESA Earth Explorer, will be the first mission designed to monitor the actual photosynthetic activity of the terrestrial vegetation. FLEX will fly in tandem with the Sentinel-3 satellite in order to make use of its payload for atmospheric characterization and thermal measurements. The nominal view of the instrument aboard FLEX, in fact, will coincide with the swath of the nadir looking camera of the Ocean and Land Colour Imager (OLCI) sensor aboard Sentinel-3 (S-3) (camera 4). FLEX will provide a completely new possibility to assess the dynamics of actual photosynthesis through SIF, offering a great advancement over current fluorescence-capable satellites because of its high spatial resolution (300 m $\times$ 300 m), coupled with a high spectral resolution over the full spectral range of fluorescence emission and xanthopyll-sensitive region. The payload for the FLEX mission will be represented by FLORIS, a two modules sensor (FLORIS-HR and FLORIS-LR): FLORIS-HR will have a spectral resolution of $\approx$ 0.3 nm around the oxygen absorption bands and a Spectral Sampling Interval (SSI) of $\approx$ 0.1 nm, while FLORIS-LR will provide a medium spectral resolution of about 2 nm with an SSI of $\approx$ 0.65 nm over the 500–780 nm spectral range (Drusch et al., 2017). With this spectral configuration, FLEX data will be used to characterize both fluorescence and Non-Photochemical Quenching (NPQ), with great flexibility to compute a range of fluorescence- and reflectance-based high level products towards the retrieval of photosynthesis.

In the last years, a number of activities has been carried out by ESA to test the feasibility and usefulness of the FLEX mission. Among these, several measurements campaigns were performed using state-of-the-art hyperspectral devices specifically designed for passive fluorescence retrieval from ground (*i.e.*, the manual spectroscopy system and the Multiplexer Radiometer Irradiometer from the Laboratory of Remote Sensing of Environmental Dynamics, University of Milano-Bicocca) and airborne platform (*i.e.*, the HyPlant sensor, developed by Specim in collaboration with ESA and the Forschungszentrum Juelich). These activities set the basis for the selection of FLEX as the 8th Earth Explorer mission.

In February 2018, ESA started the new ATMOFLEX project, with the main aim of collecting Sentinel-3 measurements and collocated ground observations characterizing the state of the atmosphere for an extended period of time. Within

the context of this project, several sites have been instrumented with state-of-the-art hyperspectral spectroradiometers (FLOX; J&B Hyperspectral Devices, Germany) continuously measuring over the vegetation. The FLOX houses two high resolution spectrometers in the Visible and Near InfraRed (VNIR) spectral region, one being specifically optimized for fluorescence retrieval, measuring the incoming irradiance and upwelling radiance from the vegetation. The measurement sites spanned across Europe (Italy, Germany, France, Spain, and Switzerland), in a variety of natural and agricultural ecosystems. In addition to that, during its commissioning phase, the new Sentinel-3B satellite was flown in tandem with the operational Sentinel-3A satellite, approximately 30 seconds apart, in FLEX/S-3 like mode. For a limited period of time (*i.e.,* from 14th June 2018 to 14th August 2018), the OLCI sensor onboard Sentinel-3B was reconfigured to reflect as much as possible the future spectral resolution of the FLORIS-HR and -LR spectrometers, bringing the unique opportunity to test atmospheric correction and fluorescence retrieval methods on real satellite data at the FLEX spatial resolution of $300\,\mathrm{m} \times 300\,\mathrm{m}$. Intensive data acquisition was carried out within the ATMOFLEX project during this reconfigured phase, with the HyPlant sensor under-flying the satellites over the sites on a regular basis within the context of the FLEXSense project.

The main objective of this project (MULTI-FLEX) is to build and test flexible tools for assessing vegetation dynamics using multi-source, multi-resolution remote sensing data, in particular working on the data acquired during the FLEXSense/ATMOFLEX 2018 campaign. The specific objectives of the project are:

- to develop a processing chain for coupled retrieval of fluorescence and vegetation parameters from continuous ground hyperspectral measurements in FLEX-like spectral configuration;

- to adapt and test this inversion scheme to the spectral resolution of the reconfigured Sentinel-3B OLCI;

- to exploit HyPlant and Sentinel-2 Top Of Canopy (TOC) products to test simple metrics to explain *SIF* at $300\,\mathrm{m} \times 300\,\mathrm{m}$ spatial resolution;

- to scale the inversion scheme proposed above to the reconfigured OLCI-B TOC data.

The project was originally divided in four WPs, a fifth WP was added through a CCN as described in Section 3.1:

WP1 Development of a processing chain for coupled retrieval of fluorescence and vegetation parameters from continuous ground hyperspectral measurements;

WP2 Adaptation of the inversion scheme to the spectral resolution of the reconfigured Sentinel-3B OLCI;

WP3 Exploitation of HyPlant and Sentinel-3A TOC products to test simple fluorescence-derived metrics;

WP4 Scaling of the scheme proposed in WP2 to the reconfigured OLCI-B TOC data;

WP5 Processing of the reconfigured Sentinel-3B OLCI data to L-1b TOA radiances.

A workflow of the project including the main processing steps and interactions between the different WPs is reported in Figure 1
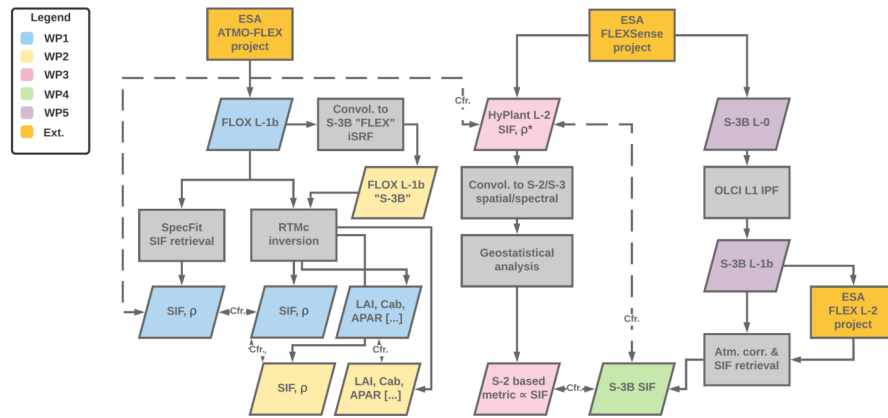

Figure 1: Workflow of the MULTI-FLEX project highlighting the connection between the different Work Packages (WPs).

3 Status of the project at final review

3.1 Deviation from the proposal

The major deviation from the proposal regards the processing of the reconfigured Sentinel-3B (S-3B) data acquired during the 2018 FLEXSense campaign. The data acquisition was successful, and the data were declared available and exploitable for this project. However, the processing of the satellite data obtained with the reprogrammed OLCI instrument on Sentinel-3B represented a challenge, since no ground processor capable of dealing directly with these raw data was available. In fact, the peculiar spectral configuration used to mimic as much as possible the FLEX optical payload was achieved modifying one of the spectral calibration mode of the OLCI spectrometer onboard S-3B (*i.e.*, S09 calibration mode). S09 raw data are used for calibration purposes and are not routinely processed to Top Of Atmosphere (TOA) radiances (*i.e.*, to Level-1 (L-1)). Therefore, in order to make use of this dataset, a new work package

(WP5) was added to the initial proposal for the processing of S-3B OLCI data acquired in FLEX mode from Level-0 (L-0) to L-1b. The activity was formalized in a Contract Change Notice (CCN) (Contract No. 4000125442/18/I-NS), and performed during a 6 months stay at ESA-ESTEC (from 1st February 2019 to 31st July 2019). Details about the processing and results are reported in Section 3.2.5 and Section 3.3.5. The atmospheric correction of these data, a necessary step to perform the activities initially foreseen in WP4 of this project, was foreseen through a collaboration with the FLEX Level-2 study team. Unfortunately, this was not possible due to a change in the schedule of the FLEX Level-2 study. The "FLEX mode" S-3B data, in fact, will be used only within the coming phase of the project. Hence, a simplified bottom-up approach was followed to compare HyPlant and S-3B data in one of the campaign sites (Section 3.2.4, Section 3.3.4). Moreover, tests performed in WP2 showed that the spectral resolution of the "FLEX mode" S-3B data is not sufficient to perform the numerical inversion of a complex Radiative Transfer Model (RTM) as defined in WG1. In addition to that, the activities foreseen in WP3 were partially adjusted to define quantitative protocols for SIF spatial sampling towards a validation strategy for medium resolution (and in particular FLEX) SIF satellite products. In this regards, HyPlant data were used to define the optimal number of proximal sensing measurements needed to characterize the spatial variability of the SIF signal at the FLEX pixel scale. More details on the processing and results of this activity are reported in Section 3.2.3 and Section 3.3.3, respectively.

3.2 Material and methods

In this section the material and methods of the activity performed at final review are reported. For consistency with the proposal, the activity is divided in the different WPs, for their interaction please refer to Figure 1.

3.2.1 WP1

The FLOX system   The FLOX is an automatic ground spectroscopic system specifically designed to retrieve fluorescence in the O_2-A (centered at 760 nm) and O_2-B (centered at 687.0 nm) absorption bands using a high-resolution QE Pro spectrometer (OceanOptics, Dunedin, USA) covering the spectral range 650–800 nm with a SSI of 0.17 nm and a Full Width at Half Maximum (FWHM) of 0.3 nm), and VNIR reflectance with the Flame spectrometer (OceanOptics) covering a wavelength range of 400–950 nm with a SSI of 0.65 nm and a FWHM of 1.5 nm). Each spectrometer has two channels - one for down-welling irradiance and one for up-welling radiance with a Field Of View (FOV) of 25°. Each acquisition cycle consisted of a series of measurements:

1. down-welling irradiance;

2. up-welling radiance;

3. second down-welling irradiance;

4. dark current (DC) measurements for the two channels.

The second down-welling irradiance measurement allows accounting for the stability of illumination conditions for the subsequent data quality control. Thanks to the quick electronics and optical shutters, each acquisition cycle is acquired and saved in less than 1 minute. An example of measurement cycle is reported in Figure 2.
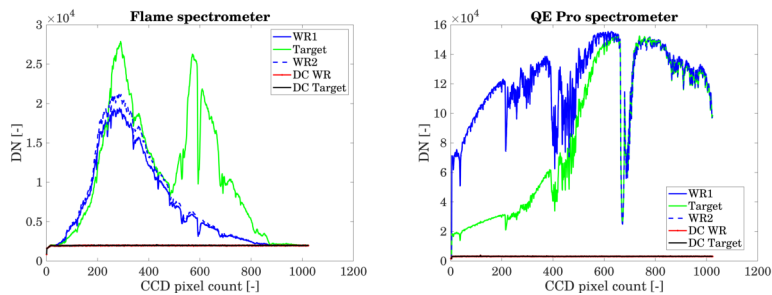

Figure 2: Measurement cycle of the FLOX system.

7

Data availability and preprocessing   High temporal resolution time series of hyperspectral radiance/irradiance were collected over different targets within the context of the 2018 ESA ATMO-FLEX campaign.

The FLOX data were filtered by means of several quality criteria, in particular:

- saturation of one or more spectra within a cycle;

- relative difference between the first and the second measurements of incoming radiation within a cycle

  - less than 1% over the full spectrum for the QE Pro;

  - less than 10% over the full spectrum for the Flame;

- Sun Zenith Angle (SZA) $\leq 50°$

Moreover, after applying the above-mentioned filtering criteria, only data acquired within 15 minutes from solar noon were selected for further analysis.

Radiance-based fluorescence retrieval   Top of canopy SIF was retrieved in the O_2-A and O_2-B oxygen absorption bands using state of the art spectral fitting methods (SFM; Cogliati et al. 2015), originally proposed by Meroni and Colombo (2006) and Meroni et al. (2010). This method models the fluorescence and the true reflectance (ρ; *i.e.*, the ratio of the reflected radiance and the incoming radiance) as a function of wavelengths inside the O_2-A and O_2-B oxygen absorption bands. SIF^{SFM} and ρ^{SFM} were modeled using Voigt functions and piecewise cubic splines, respectively. Moreover, the SpecFit algorithm as described in Cogliati et al. (2019) was applied to retrieve the full spectrum of the SIF emission ($SIF^{SpecFit}$) in the spectral range 670–780 nm. The method was adapted to the FLOX spectral resolution and it is now publicly available (`https://gitlab.com/ltda/flox-specfit`). The integral of each SIF spectrum ($SIF_{int}^{SpecFit}$) was computed by means of trapezoidal numerical integration.

Coupled retrieval of fluorescence and vegetation parameters   The model inversion routine for the retrieval of biophysical and biochemical parameters of the vegetation was based on a non-linear least squares Numerical Optimization (NO) algorithm that minimizes the differences between the measured and the modeled apparent reflectance (ρ^*) in the spectral region 400–900 nm. The methodology relies on the numerical inversion of a simplified version of the Soil Canopy Observation, Photochemistry and Energy fluxes (SCOPE) model (Tol et al., 2009), as presented in Celesti et al. (2018). In summary, radiance spectra from the Flame and QE Pro spectrometers were merged together in order to obtain a single spectrum with the highest possible spectral resolution (Figure 3). However, the retrieval scheme had to be adapted in order to accommodate for the different spectral resolution of the FLOX compared to the system

used by Celesti et al. (2018). In particular, it was necessary to apply a weighting scheme to take into account the lower spectral resolution of the FLOX in the oxygen absorption bands and drive the optimization of the fluorescence-emitting model (Figure 4). Moreover the inversion routine was parallelized and optimized in order to get a computational speed improvement of about 20 times, mandatory to deal with the large number of measurement cycles acquired by the FLOX every day ($\approx$ 600).

Table 2: Lower boundaries (LB), upper boundaries (UB), *a priori* values (p_0), assumed standard deviations (σ_{p_0}) and starting values (SV) of each retrieved parameter. Free parameters include six Fluspect-B parameters for Chlorophyll (C_{ab}) and carotenoids (C_{car}), leaf dry matter (C_{dm}), water content (C_w) and senescent material (C_s), and fluorescence quantum efficiency (fqe, equivalent to Φ_F), the Leaf Area Index (LAI) from the SAIL model, and the volumetric soil moisture percentage in the root zone (SMp) from the GSV model.

Parameter	Unit	LB	UB	p_0	σ_{p_0}	SV
C_{ab}	$\mu g\,cm^{-2}$	0	100	40	30	40
C_{car}	$\mu g\,cm^{-2}$	0	30	10	10^9	10
C_{dm}	$g\,cm^{-2}$	0	0.04	0.01	10^9	0.005
C_w	cm	0	0.05	0.01	10^9	0.02
C_s	-	0	0.4	0.15	10^9	0.1
fqe (Φ_F)	-	0	1	0.01	10^9	0.01
LAI	$m^2\,m^{-2}$	0	6	2	1	3
SMp	%	5	55	30	10^9	30

A number of parameters were left free to vary during the inversion routine. In particular, six Fluspect-B parameters for Chlorophyll (C_{ab}) and carotenoid content (C_{car}), leaf dry matter (C_{dm}), water content (C_w), senescent material (C_s), the fluorescence quantum efficiency (fqe), and the Leaf Area Index (LAI) from the SAIL model. SMp is a parameter in the GSV model for the volumetric soil moisture percentage in the root zone, and it was left free to account for potential variations in the soil brightness due to soil moisture content. The Fluspect-B parameter "fqe" corresponds to the fluorescence emission efficiency (Φ_F). In order to test the retrieval scheme in a generally applicable configuration, the lower (Table 2, column LB) and upper boundaries (column UB) of the free parameters were left very wide. A spherical leaf angle distribution (LIDFa = -0.35; LIDFb = -0.15), was chosen as a generic starting point for modelling the canopy.

3.2.2 WP2

Convolution of spectral data   In oder to test the feasibility of different retrieval approaches on the reconfigured S-3B OLCI data, the high resolution
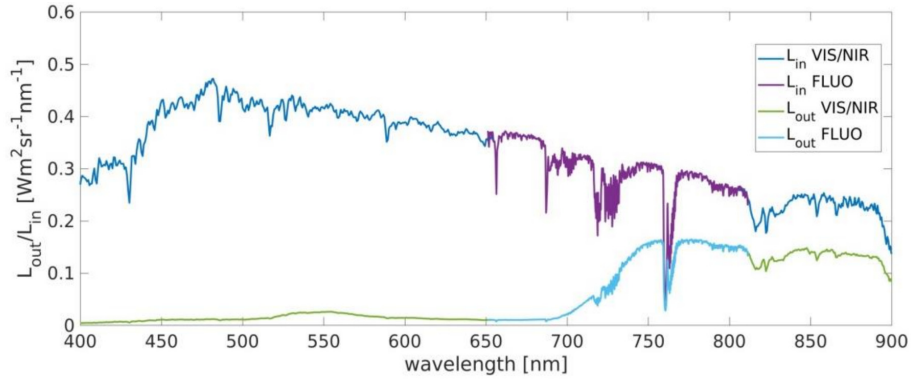
Figure 3: Example of the spectra from the Flame and QE Pro merged in order to be used for the numerical inversion.
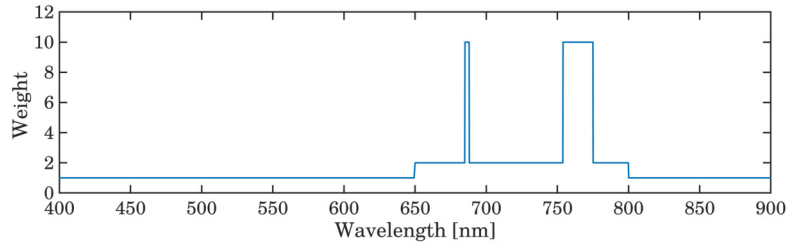

Figure 4: Weight function used in the numerical inversion of the FLOX data.

VNIR FLOX radiance (*i.e.*, obtained merging the QE Pro and the Flame spectral data as described in Section 3.2.1) data were convolved to the instrument Spectral Response Function (iSRF) of the "FLEX mode" OLCI data. Figure 5 shows an example of a high resolution VNIR FLOX spectrum of incoming radiance at full resolution and convolved to the reconfigured S-3B OLCI "FLEX mode" iSRF.

SIF **retrieval**   *SIF* was retrieved from the convolved spectra using the Spectral Fitting Methods (SFM) (Cogliati et al., 2015; Meroni et al., 2010) and SpecFit (Cogliati et al., 2019) methods. These methods are generally applied to hyperspectral data characterized by a higher spectral resolution for *SIF* retrieval in the O_2-A and O_2-B bands, and over the full spectrum of emission, respectively. Nevertheless, their application to the S-3B OLCI "FLEX mode" data was tested

10
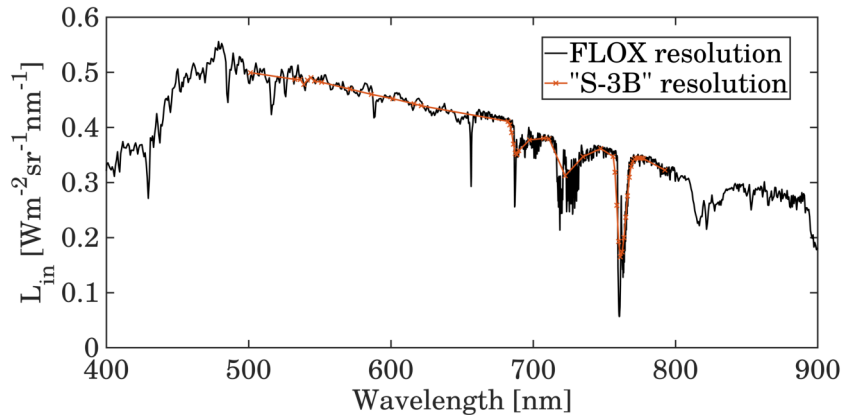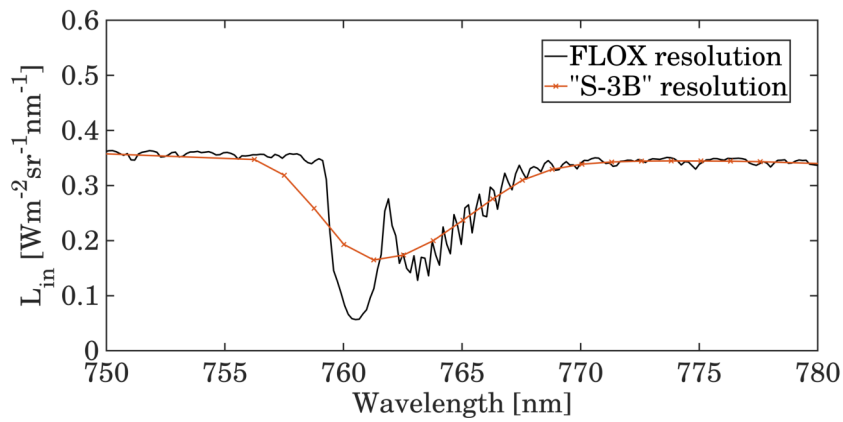
Figure 5: a) Example of a high resolution VNIR FLOX spectrum of incoming radiance at full resolution and convolved to the reconfigured S-3B OLCI "FLEX mode" iSRF; b) a zoom centered on the O_2-A band.

and compared with the reference values obtained from full spectral resolution FLOX measurements.

3.2.3 WP3

HyPlant SIF **maps** SIF maps were obtained applying SFM to HyPlant "FLUO" radiance images collected in Selhausen (Germany) and Braccagni (Italy) during the FLEXSense 2018 campaign. The FLUO module onboard HyPlant is a high spectral resolution module specifically devoted to the retrieval of SIF. It covers the 670–780 nm spectral range with a FWHM of ≈ 0.3 nm and a SSI of

0.11 nm enabling the retrieval of both red and far-red SIF. Both sites present a mostly agricultural heterogeneous landscape with a variety of crops. In particular, data collected on 26th June 2018 in Selhausen and on 30th July 2018 in Braccagni were used. Images were acquired at different flight altitudes varying between 600 m and 3050 m, corresponding to a spatial resolution between 1 m and 4.5 m. In this analysis, SIF maps retrieved in the O_2-A band (SIF_{760}) were used to represent both proximal sensing and satellite measurements. In this way, only the uncertainty related to the spatial sampling was selectively tackled. At the same time this provided the opportunity to work on real scenarios with a real spatial heterogeneity. All images were aggregated to 9 m $\times$ 9 m spatial resolution by means of averaging kernels before performing any other analysis in order to be consistent one with the other.

Spatial data sampling: homogeneous fields   At first, the analysis was performed on homogeneous agricultural fields in both Selhausen and Braccagni. The boundaries of selected fields were taken from a land cover map of the sites, and integrated with manual digitization as necessary. In total, 31 fields were selected in Selhausen and 30 in Braccagni. Figure 6a shows the fields selected in Selhausen. The size of the homogeneous fields ranged between 28 000 and 97 000 m^2 including bare soils, sugar beet, barley, and pea fields in Selhausen, while in Braccagni fields were much larger ranging between 60 000 and 300 000 m^2 with wheat, barley and chickpea being the most represented land covers.

9 m $\times$ 9 m pixels of the HyPlant SIF maps within each field were used as a proxy of the footprint of the proximal sensing measurements. These values were compared to the aggregated (average) value of all pixels within the field ($\mu_{SIF_{760}^{field}}$). 200 fully random points were selected in each field to simulate a random spatial sampling (Figure 6b). A 10 m minimum distance between points was imposed in order to avoid selecting the same pixel more than once.

Statistical analysis: random selection   The absolute deviation between the mean of the sampled points and the mean of the entire field was used to determine the representativeness of the sampling (ADM):

$$ADM = \left| \frac{\sum_{n=1}^{npts} SIF_{760,n}^{points}}{npts} - \mu_{SIF_{760}^{field}} \right| \tag{1}$$

where $npts$ is the number of sampling points and varies from 1 to 200. A step of 1 point was used for cases between 1 and 15 points, a step of 2 from 16 to 60 and a step of 4 from 64 to 200, for a total of 73 sampling cases. In order to avoid potential biases related to the random selection (*i.e.*, when selecting by chance a point "too close" or "too far" from the mean of the field), each case was repeated 200 times following a bootstrap approach. These repetitions were then summarized computing the mean and the standard deviation of ADM obtained for each sampling case (μ_{ADM} and σ_{ADM}, respectively).

(a)   (b)
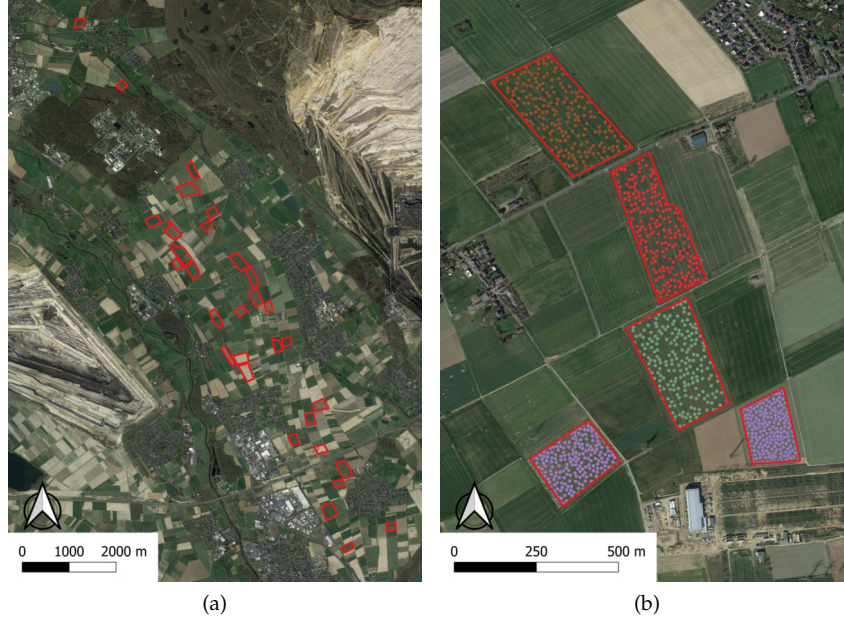
Figure 6: a) ; b) .

Three arbitrary thresholds were defined to evaluate the number of points required to sufficiently characterize the fluorescence of each field, 0.2, 0.15 and $0.1 \, \mathrm{mWm^{-2}sr^{-1}nm^{-1}}$, respectively. Finally, the minimum number of sampling points for which $\mu_{ADM} + \sigma_{ADM}$ was lower than the threshold was extracted.

Spatial data sampling: FLEX pixels   11 and 48 FLEX pixels were digitized in Selhausen and Braccagni, respectively. The same procedure applied to the homogeneous fields was replicated for the FLEX pixels. Figure 7 shows the FLEX pixels and the associated 200 random points in Selhausen.

Statistical analysis: linear mixing   Given the potential mixture of different components (*i.e.*, different land covers) within the FLEX pixel in *e.g.*, agricultural landscapes, a linear mixing model was applied to the sampled values:

$$\mu^{lmix}_{SIF^{points}_{760}} = \left(\sum_{n=1}^{nlc} fc_{lc}(n) * \mu_{SIF^{points}_{760}}(n) \right) + \left(1 - \sum_{n=1}^{nlc} fc_{lc}(n) \right) * \frac{\sum_{n=1}^{nlc} \mu_{SIF^{points}_{760}}(n)}{nlc}$$

(2)

where nlc is the number of land covers within the FLEX pixel that are sampled (*i.e.*, only the components that are actually sampled for each sampling case) and fc_{lc} is the fractional cover of the each land cover within the FLEX pixel. In the
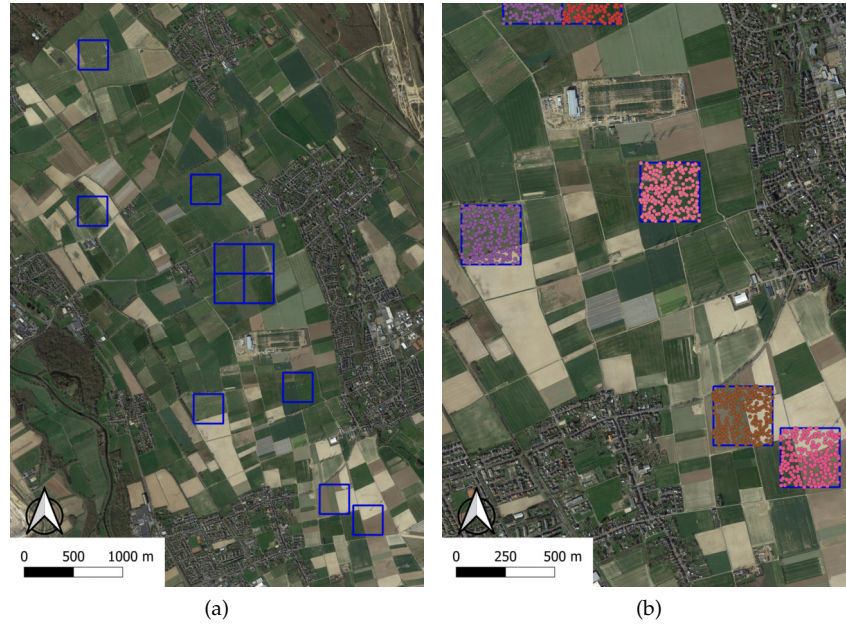
13

Figure 7: a) ; b) .

first half of Equation (2) a linear model based on fc_{lc} is applied to the sampled values, so that each group of points within a land cover was weighted for the fractional cover of the land cover in the FLEX pixel. Wherever one or more land covers are not included in the sampling (*e.g.*, in cases with fewer sampling points than land covers), in the second half of Equation (2) a compensation factor is applied by multiplying the remaining fc by the average values of the sampled points.

Statistical analysis: stratified random sampling   In order to further improve the effectiveness of the spatial sampling of the FLEX pixel, a stratified random approach was tested, with and without applying the linear mixing to the selected points. The rationale followed to apply this scheme for varying number of sampling points (*npts*) and land covers within the FLEX pixel (*nlc*) is reported below.

$nlc = 1$ easiest case, points are selected incrementally for each case within the only land cover, the linear mixing model is not even applied

$nlc > 1$ points are selected according to the following rules:

$npts = 1$ the point is selected randomly among the ones within the land cover with the highest fractional cover within the FLEX pixel

14

$1 < npts <= nlc$ the points are selected randomly among the ones within the land covers with the highest fractional cover within the FLEX pixel, *i.e.*, if $npts = 2$ and $nlc = 3$ a single point for each land cover is selected among those within the two land covers with the highest fractional cover within the FLEX pixel

$npts > nlc$ the pixels are distributed among the different land covers proportionally to the fractional cover within the pixel of each land cover

Sentinel-2 surface reflectance metrics to describe SIF_{760} at the FLEX spatial resolution HyPlant surface reflectance data are obtained from atmospheric correction of the at-sensor radiance acquired with the DUAL sensor (Siegmann et al., 2019). This sensor covers the visible as well as the near and shortwave infrared portions of the electromagnetic spectrum (380–2500 nm) with a FWHM between 3.65 and 10.55 nm and a SSI between 1.71 and 5.58 nm. Sentinel-2 (S-2) Level-2 (L-2) data were simulated starting from HyPlant surface reflectance by convolution to the S-2 spectral resolution and spatial grid. In particular, a 20 m grid was selected, and only bands B2, B3, B4, B5, B6, B7, B8a, B11 and B12 were reconstructed (Table 3).

Band	Central wl [nm]	FWHM [nm]
B2	492.4	66
B3	559.8	36
B4	664.6	31
B5	704.1	15
B6	740.5	15
B7	782.8	20
B8a	864.7	21
B11	1613.7	91
B12	2202.4	175

Table 3: Spectral characteristics of the Sentinel-2 spectral bands reconstructed from HyPlant surface reflectance.

SIF_{760} maps for the area were retrieved from HyPlant FLUO at-sensor radiance data by means of SFM (Cogliati et al., 2018). A number of Vegetation Indices (VIs) was computed from the S-2-like data reconstructed from HyPlant, including the Normalized Difference Vegetation Index (NDVI) (Figure 8c; Tucker 1979) and the Near InfraRed reflectance of terrestrial vegetation (NIRv) (Figure 8e; Badgley et al. 2019). The coefficient of variation (CV) of the S-2 surface reflectance spectra was also computed per pixel ((**??**)) as the average CV for all spectral bands (Tagliabue et al., 2020):

$$CV = \frac{\sum_{b=1}^{n} \frac{sd(\rho_b)}{mean(\rho_b)}}{n} \quad (3)$$

where $sd(\rho_b)$ and $mean(\rho_b)$ are the standard deviation and the mean of band b and n is the number of spectral bands.

The VIs maps, together with the CV and SIF_{760} ones, were then aggregated to the FLEX spatial grid (*i.e.*, 300 m $\times$ 300 m; Figures 8b, 8d, 8f).
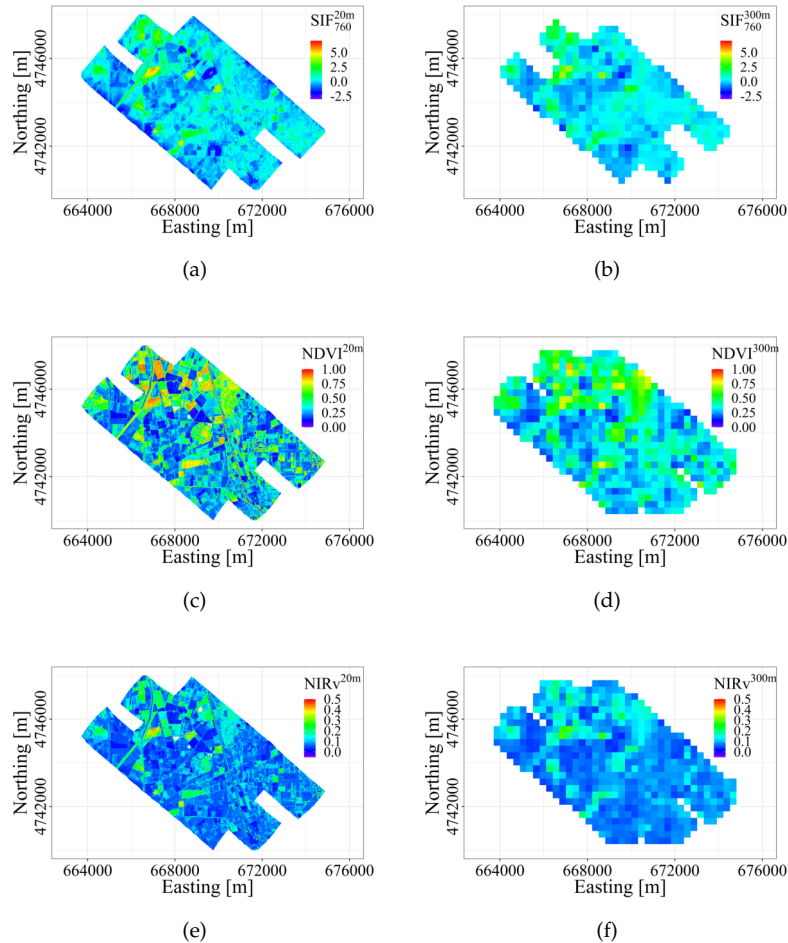

Figure 8: SIF_{760}, NDVI and NIRv maps of the study area in Braccagni (Italy) at 20 m and 300 m spatial resolution.

3.2.4 WP4

HyPlant TOC products   As described in Section 3.1, it was not possible to realize a full atmospheric correction of the S-3B "FLEX mode" products L-1b (see Section 3.2.5 for a description of the L-1b data). Nevertheless, in order

to perform an initial step towards the full exploitation of these data, a proof-of-concept of a bottom-up approach starting from HyPlant surface reflectance data was achieved. In particular, HyPlant data acquired on 30th July 2018 at 3050 m over the Braccagni site in Italy were used. Figure 9 shows an RGB synthesis of the mosaic of HyPlant surface reflectance at the original spatial resolution (*i.e.*, 4.5 m × 4.5 m; Figure 9a) and after resampling to the spatial grid of S-3B (*i.e.*, ≈ 300 m × 300 m; Figure 9b).

(a)   (b)
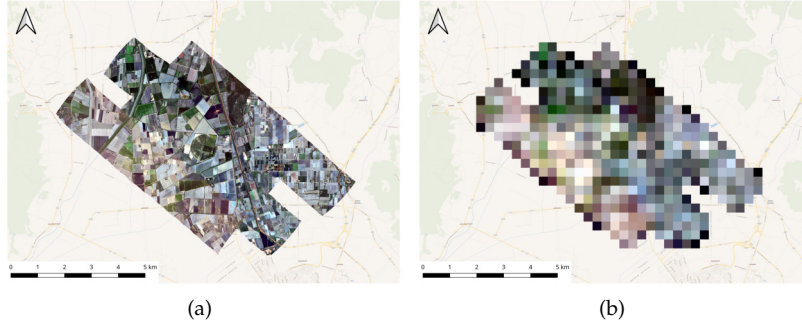
Figure 9: RGB synthesis of HyPlant surface reflectance maps of the study site in Braccagni (Italy) a) at the original spatial resolution (*i.e.*, 4.5 m × 4.5 m) and b) after resampling to the spatial grid of S-3B (*i.e.*, ≈ 300 m × 300 m).

Bottom-up approach The radiative transfer function used to simulate TOA radiance is adapted from Cogliati et al. (2015) and it is reported in Equation (4):

$$L_{TOA}^{sim} = t_1 \left[t_2 + t_8 r_{so} + \frac{t_9 r_{so} + t_{10} r_{sd}}{1 - r_{dd} t_3} + \frac{t_{11} r_{dd}}{1 - r_{dd} t_3} \right] \qquad (4)$$

r_{so}, r_{sd} and r_{dd} are the target hemispheric-directional reflectance factor (HDRF), the spatially filtered directional-hemispherical reflectance factor (DHRF) of the surrounding and the spatially filtered bi-hemispherical reflectance (BHRF) of the surrounding, respectively. In this case, a lambertian case with no adjacency effect was simulated, assuming r_{so}, r_{sd} and r_{dd} to be all equal to the HyPlant surface reflectance. The "t-terms" in the equation are atmospheric functions computed at high spectral resolution by means of the MODerate resolution atmospheric TRANsmission (MODTRAN) radiative transer code before the convolution to the the sensor spectral bands (Verhoef et al., 2014). The atmospheric parameters for running MODTRAN were derived from the ancillary meteorological data contained in the S-3B L-1b products, and from ancillary ground data. L_{TOA}^{sim} was convoluted to the spectral bands of S-3B by means of gaussian kernels. Then, L_{TOA}^{sim} was compared to S-3B TOA radiance measurements (L_{TOA}^{S-3B}) computing the per-pixel spectral Pearson's linear correlation coefficient:

$$rho(x,y) = \frac{\sum_{i=1}^{n}(L_{TOA,x,y,i}^{sim} - \overline{L_{TOA,x,y}^{sim}})(L_{TOA,x,y,i}^{S-3B} - \overline{L_{TOA,x,y}^{S-3B}})}{\sqrt{\sum_{i=1}^{n}(L_{TOA,x,y,i}^{sim} - \overline{L_{TOA,x,y}^{sim}})^2(L_{TOA,x,y,i}^{S-3B} - \overline{L_{TOA,x,y}^{S-3B}})^2}} \quad (5)$$

with (x, y) being the relative image coordinates (not geographic) of each pixel, and n being the number of spectral bands. In addition to that the λ agreement index proposed by Duveiller, Fasbender, and Meroni (2016) was tested.

S-3B data were filtered using the quality flags stored in the L-1b products. In particular, `'saturated'`, `'bright'` (*i.e.*, a proxy for clouds), `'dubious'` or `'invalid'` pixels were removed.

3.2.5 WP5

Data availability   During the Sentinel-3A (S-3A)/S-3B tandem phase, OLCI (on the B unit) was operated in a FLEX-like mode covering a different spectral range in 45 bands. In total, 24 acquisitions were taken in this mode, each covering stripes with more than 1500 km along track. The acquisitions areas of the core ATMO-FLEX campaign sites in the USA, Switzerland, France, Italy and Germany were all covered. Access to L-0 data and to Ancillary Data File (ADF) was granted through the S-3 Commissioning Server.

L-0 to L-1 processing   The overall data processing strategy was based on the use of the S-3 L-1 Earth Observation (EO) mode data processor (OL1) available at ESA-ESTEC. This processing was not straightforward because the OL1 processor is not made for dealing with the FLEX-like OLCI data. In order to overcome this without modification to the OL1 processor code, two methods were defined together with the S-3 project team:

1. reshape the L-0 data in order to mimic the structure of the nominal OLCI data and feed the OL1 processor with them without modifying the code;

2. feed the OL1 processor directly with full FLEX-like data testing if it works for a generic number of bands.

Option 2 was discarded after an early evaluation due to the discrepancies between the calibration mode data and the EO mode data, that would have been rejected by the quality checks in the OL1 processor. Hence, Option 1 was taken forward with the support of the S-3 Mission Performance Center (MPC), and in particular of Ludovic Bourg and Alexis Deru (ACRI-ST, Sophia Antipolis, France). The practical steps performed in order to successfully process the OLCI "FLEX mode" data were:

- definition of three optimal spectral subsets of 21 bands from the original 45;

- split of the Instrument Source Packets (ISPs) in the three spectral subsets and adaption of the headers;

- preparation of specific sets of ADFs (*i.e.*, OL_1_PRG_AX, OL_1_INS_AX and OL_1_CAL_AX) for the three subsets;

- preparation of configuration files and full set of ADFs for processing the 24 acquisitions.

The three spectral subsets (FX1-3, Figure 10) were selected according to three rules:

- maximise the overall spectral range;

- ensure a fine and regular spectral sampling in order to assure the best possible performance of the stray light correction;

- include some bands common to the three subsets.
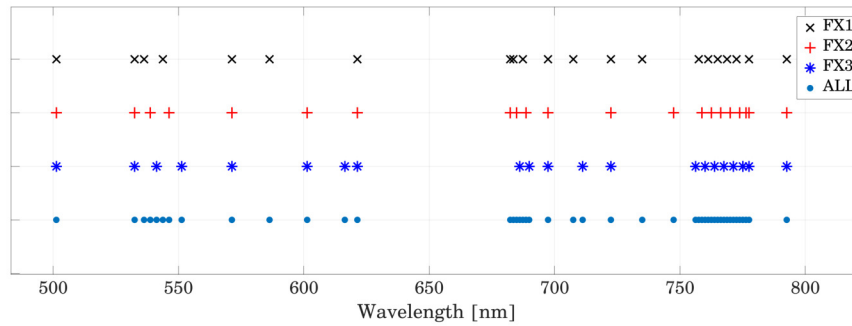
Figure 10: Definition of the three spectral subsets (FX1-3) of Sentinel-3B OLCI in "FLEX mode".

Quality evaluation   In order to evaluate the sensitivity to spectral sampling of the stray light correction module in the OL1 processor, the data distribution functions of the bands common to the three spectral subsets were compared by means of quantile-quantile (Q-Q) plots. Moreover, L-1b data in "FLEX mode" were compared with standard OLCI L-1b data from S-3A.

Per-pixel and per-band quality flags were obtained directly from the processed S-3 L-1b products and used to filter the corresponding bands in the different spectral subsets before further evaluation of the products.

3.3 Results

In this section the results of the activity performed at mid-term review are summarized. For consistency with the proposal, these are divided in the different WPs, for their interaction please refer to Figure 1.

3.3.1 WP1

Figure 11 shows the FLOX derived time series of SIF values integrated over the entire retrieval range (SIF_{int}), obtained from the SpecFit algorithm (top panel, $SIF_{int}^{SpecFit}$) and from the RTM numerical inversion (bottom panel, SIF_{int}^{RTM}). These values are obtained from the analysis of data coming from the site in Braccagni (Italy). The different colours indicate the different crops sampled during the season. The phenological trends are generally maintained between the reference retrieval (SpecFit) and the one proposed in this study, while absolute values are overestimated. In particular, the largest discrepancies occur during the forage growing phase and at the beginning of the corn growth. Both these conditions are characterized by a low fractional cover, suggesting an improper parametrization of the modelled soil reflectance and a consequent misrepresentation of the vegetation reflectance (and apparent reflectance). The overall slight overestimation of the SIF_{int}^{RTM} values is confirmed in Figure 12. The scatter plot shows a good overall agreement between the two retrieval methods, with a R^2 of 0.88. At the same time the RMSE is relatively high ($138.09 \, \mathrm{mW \, m^{-2} \, sr^{-1}}$). Crop specific linear trends suggest a potential incorrect representation of the different leaf angle distribution functions (LADf) of each crop. This might be due to the low degree of freedom left to the numerical inversion routine in the tuning of this parameter during the optimization loop. LADf, in fact, impacts substantially the radiative transfer of SIF at canopy level, and varies strongly during the phenological cycle of the crops. Additional test with more degrees of freedom in the LADf retrieval will be performed in order to overcome this limitation and improve the flexibility of the RTM-based retrieval.

3.3.2 WP2

Figure 13 shows the scatter plots and the linear regression models between SIF values retrieved from full resolution "FLEX like" FLOX data, and from FLOX data convolved to the "FLEX mode" S-3B OLCI spectral resolution in the O_2-A and O_2-B oxygen absorption bands. Both SFM and SpecFit retrieval methods were tested. In the O_2-A band, although there is an overestimation due to the different spectral resolution (a critical factor in the absorption bands where SIF is retrieved), there is a good overall agreement between the values retrieved with both SFM and SpecFit methods (upper panels). A similar overestimation has already been observed when comparing SIF retrieval from field spectrometers with different spectral resolution (Julitta et al., 2016). While the retrieval in the O_2-A seems reasonable, the O_2-B band is more critical in this spectral
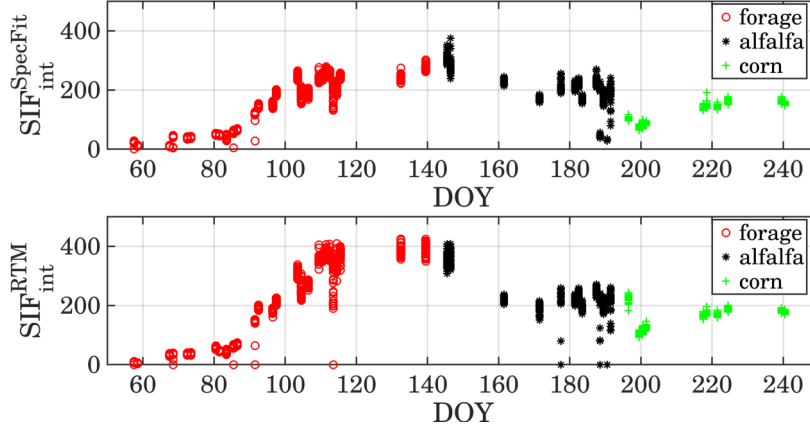
Figure 11: FLOX derived time series of *SIF* values integrated over the entire retrieval range (SIF_{int}), obtained from the SpecFit algorithm (top panel, $SIF_{int}^{SpecFit}$) and from the RTM numerical inversion (bottom panel, SIF_{int}^{RTM}). The different colours indicate the different crops sampled during the season.
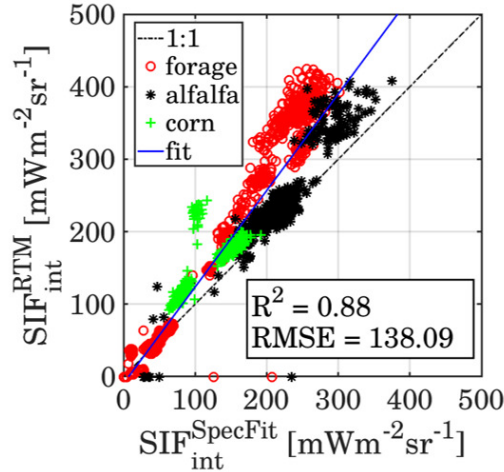

Figure 12: Scatter plot and linear regression model of the FLOX derived *SIF* values integrated over the entire retrieval range (SIF_{int}), obtained from the SpecFit algorithm ($SIF_{int}^{SpecFit}$) and from the RTM numerical inversion (SIF_{int}^{RTM}). The different colours indicate the different crops sampled during the season.

configuration. In fact, it is well known that simple retrieval approaches (*e.g.*, the FLD) do not work well in the O_2-B band due to the sharp variation in the

apparent reflectance in the red/red-edge transition. At the same time, a higher spectral resolution than the one provided by the "FLEX mode" S-3B OLCI data is required for applying complex retrieval methods (*e.g.*, iFLD, SFM). SFM retrieval did not converge in the O_2-B, probably due to the insufficient number of spectral bands. SpecFit, in turn, did converge, but the results are not comparable with the reference values both in relative and in absolute values (data not shown). This would open a potential interest for process-based retrieval capable of exploiting the inherent link between vegetation parameters and the overall (full-range) SIF emission, being not possible to rely only in the informative content of each absorption band.
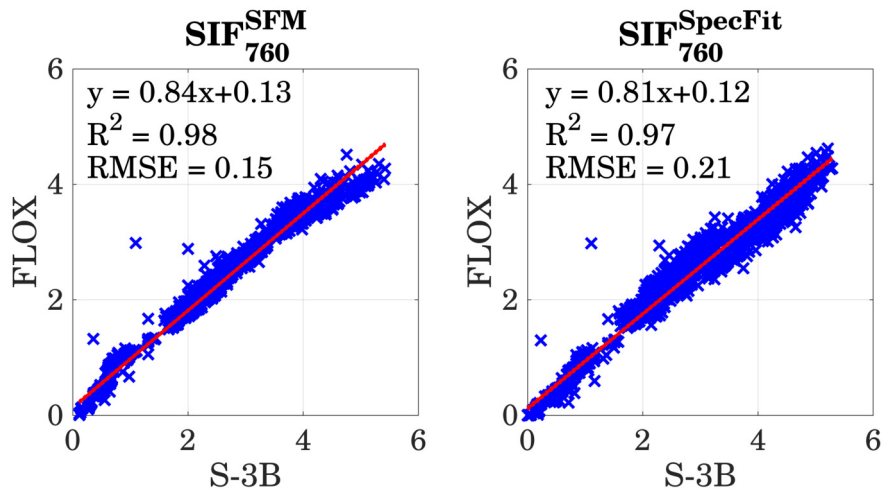

Figure 13: Scatter plot and linear regression model between $SIF_{760}^{SpecFit}$ and SIF_{760}^{SFM} retrieved from full resolution "FLEX like" FLOX data and from FLOX data convolved to the "FLEX mode" S-3B OLCI spectral resolution.

3.3.3 WP3

Homogeneous fields Figure 14 shows the variation of the mean plus standard deviation of ADM for increasing number of random sampling points in four homogeneous fields in Selhausen. Only sampling cases up to 60 points are showed in the plots because low additional accuracy is gained when further increasing the number of points. Overall, between 1 and 9 points were needed to reach the $0.2\,\mathrm{mWm}^{-2}\mathrm{sr}^{-1}\mathrm{nm}^{-1}$ threshold in the 31 homogeneous fields, with a single field reaching the threshold with 15 points (Figure 15a). A similar result is obtained in Braccagni, but the overall number of sampling points needed to reach the $0.2\,\mathrm{mWm}^{-2}\mathrm{sr}^{-1}\mathrm{nm}^{-1}$ threshold is higher (ranging from 2 to 38) due the higher heterogeneity of the fields (Figure 15b). Nevertheless, for comparable values of field SIF_{760} standard deviation ($\sigma_{SIF_{760}^{fields}}$), the threshold is reached
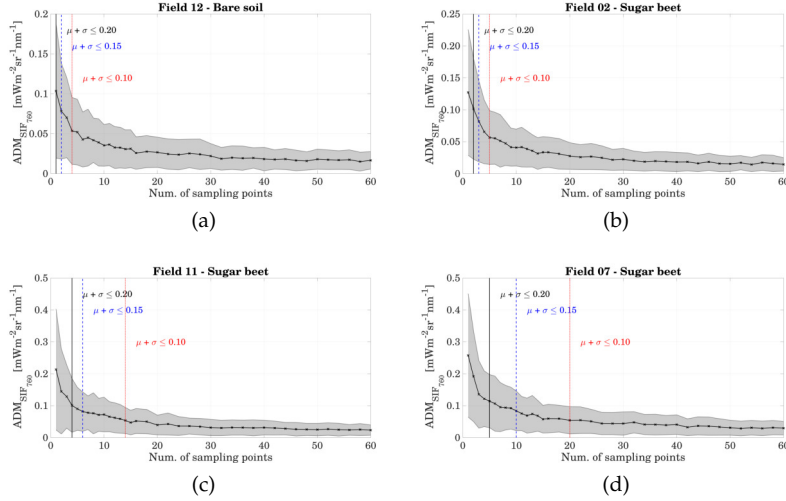
with a comparable number of sampling points.

Figure 14: Variation of the mean plus standard deviation of the absolute deviation of the mean of SIF_{760} ($ADM_{SIF_{760}^{fields}}$) for increasing number of random sampling points in four homogeneous fields in Selhausen (Germany).

FLEX pixels Figure 16 shows the number of sampling points needed to reach the $0.2\,\mathrm{mWm^{-2}sr^{-1}nm^{-1}}$ threshold for the FLEX pixels in Selhausen (a) and Braccagni (b), in relation to the standard deviation of SIF_{760} at FLEX pixel scale ($\sigma_{SIF_{760}^{FLEX}}$), applying the four different sampling approaches described in Section 3.2.3. When using a fully random sampling approach, between 5 and 32 sampling points are needed to characterize the FLEX pixel average SIF_{760} value by means of $9\,\mathrm{m} \times 9\,\mathrm{m}$ proximal sensing measurements, with a threshold of $0.2\,\mathrm{mWm^{-2}sr^{-1}nm^{-1}}$. Only FLEX pixels with a high SIF_{760} heterogeneity need more than 20 points, whereas relatively homogeneous ones need 5-15 points to be properly characterized. These numbers are generally progressively decreased when applying the linear mixing model, a stratified random sampling, or a stratified random sampling together with a linear mixing model, both in Selhausen (Figure 16a) and in Braccagni (Figure 16b).

This study exploits real data and well established and largely used field sampling strategies to provide a quantitative indication of the number of proximal sensing measurements that should be used to characterize the SIF_{760} signal within the FLEX pixel, in agricultural heterogeneous landscapes. This methodology could be scaled to lower spatial resolution products (*e.g.*, TROPOMI SIF, OCO-2 SIF), and to other ecosystems (*e.g.*, mixed and monospecific forests, tree-grass ecosystems, natural grasslands) to build a consistent strategy for SIF sampling and validation at different spatial scales.

Sentinel-2 surface reflectance metrics to describe SIF_{760} at the FLEX spatial resolution   Among the tested metrics, NIRv resulted as the best proxy for SIF_{760} variability within the FLEX pixel. Figure 17 shows the relationship between SIF_{760} values and NIRv in the study area of Braccagni (Italy). Robust linear regression models are fitted to the data, while the cell colour is linked to data density. At $20\,\text{m} \times 20\,\text{m}$ spatial resolution, the link between the two variables is relatively high (Figure 17a), but a large spread of values can be observed for all SIF_{760} intensities. At $300\,\text{m} \times 300\,\text{m}$ the relationship between average SIF_{760} and NIRv values is strongly linearized and the overall spread of both SIF_{760} and NIRv is strongly reduced. This is in line with previous observations that showed a linearization of SIF observations with temporal aggregation (Miao et al., 2020). Figure 17c and Figure 17d show the relationship between the standard deviation (*sigma*) and the interquartile range (IQR) of SIF_{760} and NIRv. Overall, a very good linear positive relationship can be observed. This is particularly relevant within the context of the future FLEX cal/val activities (*e.g.*, complementing results presented in the previous paragraph), since it would be possible to get an estimate of the expected variability of SIF_{760} within the FLEX pixel from ancillary high temporal resolution time series of S-2 surface reflectance. Within this context, more complex models based on machine learning algorithms trained on large scale, multitemporal SIF and S-2 reflectance observations could be developed in order to improve the robustness of the method.

3.3.4   WP4

Figure 18 shows the scatterplot between the TOA radiance from S-3B (L_{TOA}^{S-3B}) and the TOA radiance simulated with MODTRAN and HyPlant surface reflectance (L_{TOA}^{sim}) for four spectral bands. Overall, a good match between the two data can be observed, both in terms of correlation and of absolute values. Nevertheless, a certain number of pixels show low to very low L_{TOA}^{sim} values compared to S-3B, in particular in the green spectral region (Figure 18a, 18b), whereas in the red (Figure 18c) and in the near infrared (Figure 18d) a lower number of pixels is affected. When fitting the data with a robust linear regression model, *i.e.*, the outliers are down-weighted in the computation of the regression coefficients, a linear trend close to the identity line is found for all investigated spectral bands. The largest discrepancies are found for the green bands, were a higher impact due to the improper representation of the atmosphere can be expected.

Figure 19 shows the per-pixel Pearson's correlation coefficient (rho, Figure 19a) and lambda agreement index (λ, Figure 19b) computed between the TOA radiance from S-3B (L_{TOA}^{S-3B}) and the TOA radiance simulated with MODTRAN and HyPlant surface reflectance (L_{TOA}^{sim}). rho values are extremely high, apart from pixels at the very edge of the HyPlant mosaic that should not be considered in this analysis due to partial (incomplete) coverage of the S-3B pixel. λ values show a more heterogeneous behaviour, enhancing spectral discrepan-

cies between the two data that can be mostly attributed to spectral offsets. In fact, λ can be seen as an extension to rho that down-regulates the value of rho according to the offset encountered in the data.

Although very preliminary, this exercise strengthen the confidence on the quality of the S-3B "FLEX mode" L-1b data, paving the way for future exploitation of this dataset for land and marine application.

3.3.5 WP5

Figure 20 shows an example of the L-1b TOA radiance products obtained from the processing of the three spectral subsets of the original "FLEX mode" S-3B OLCI data. In particular, in the top panel a pseudo-RGB display of the data using the standard "OLCI L1 - Tristimulus" synthesis for one of the 24 acquisition is reported. After the processing, in fact, three standard formatted OLCI L-1b products are produced, each of them containing the information of one of the three subsets. In the bottom panels, the corresponding spectra extracted for a random vegetated pixel are plotted.

In order to quantitatively evaluate the performance of the processor in relation to the different spectral configuration of each of the three spectral subsets, the distribution functions of the microbands common to more than one spectral subset were compared. In particular, this was achieved by using quantile-quantile (Q-Q) plots between each couple of common microbands. Figure 21 shows the Q-Q plots for the image acquired on 10th July 2018. Without applying any quality filtering to the values, there was a certain discrepancy but only for very high radiance values (*i.e.*, highly reflective surfaces such as clouds). After removing the saturated pixels by means of the quality flags stored in the L-1b product, the distribution functions show a perfect match (Figure 22). This gives confidence in the fact that the OL1 processor can handle these relatively high resolution data without introducing any distortion due to the spectral configuration of the three subsets.

An additional step in the evaluation of the "FLEX mode" data was done by comparison with TOA data from S-3A. Figure 23 shows an example of a comparison between a single band of the two L-1b products for a geographical subset of the acquisition as shown in the top panel. The Q-Q plot shows a certain discrepancy for very high values, but a very good agreement for low-to-high values. This preliminary analysis was carried out without removing saturated pixels. Moreover, the spatial mismatch between the two products (co-registration) and more important the spectral resolution mismatch between the standard OLCI band and the "FLEX mode" microband were not accounted for. Given this, the overall very good agreement in the range of possible vegetation radiance values (low-to-mid range) looks promising and foster the exploitation of the S-3B data for additional quantitative analysis.

A further comparison with S-3A data was performed using a time series of concurrent observations from the two satellites during the commissioning phase. Figure 24 shows the temporal trends of TOA reflectance values for selected bands from the Sentinel-3A OLCI and the "FLEX mode" Sentinel-3B

OLCI data over the La Crau site (43.558 85° N, 4.864 472° E). TOA reflectance values were extracted in a 3 pixels x 3 pixels (*i.e.*, $\approx 900\,\text{m} \times 900\,\text{m}$) region centred on the site, and spatially averaged in order to minimise uncertainties due to the potential geolocation mismatch between OLCI A and OLCI B products. Overall a very good agreement between the different TOA reflectances is observed across the whole spectral range. In fact, not only the values from the two sensors match in terms of relative variation over time, showing in most cases a consistent shape, but the absolute values for the selected bands/microbands show a very good agreement as well. A reasonable exception to this is represented by the bands/microbands inside the O_2-A band (bottom-left and bottom-centre panels), due to the growing impact of the different FWHM of the tho products within the absorption bands.
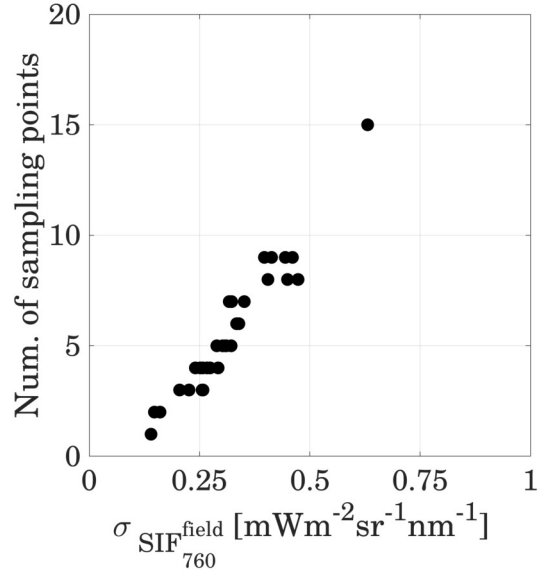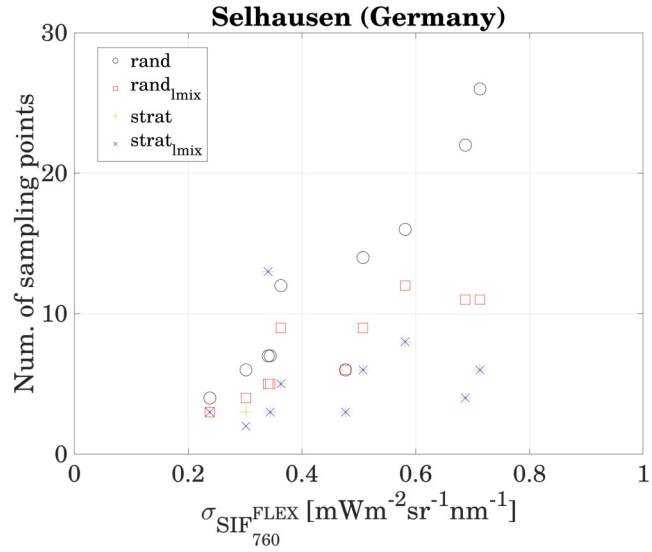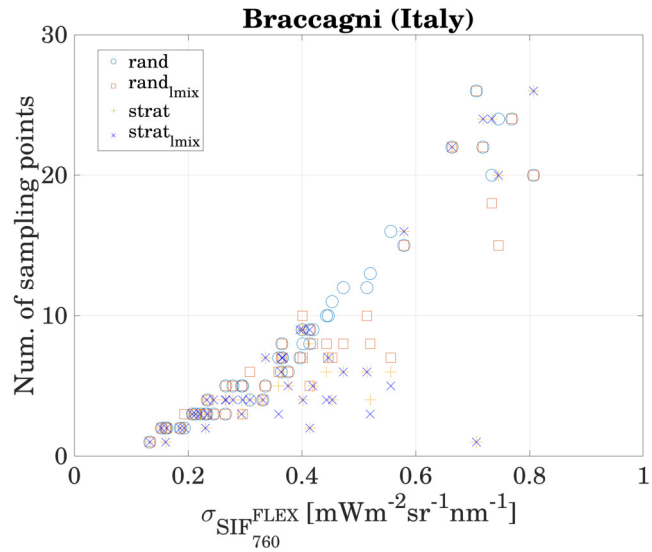
(a)
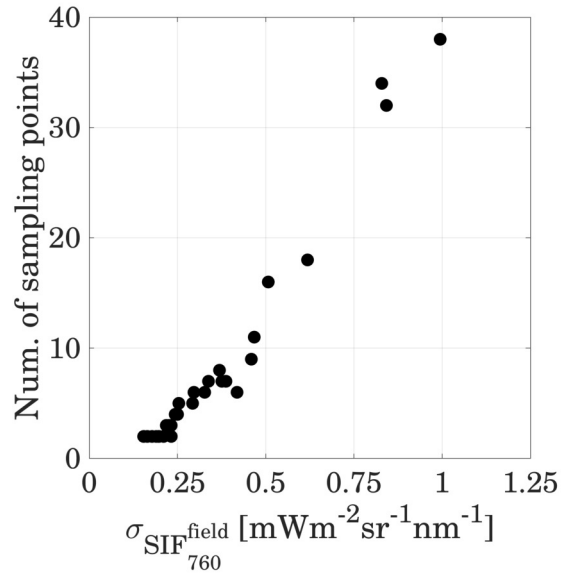
(b)

Figure 15: Number of sampling points needed to reach the $0.2\,\mathrm{mWm^{-2}sr^{-1}nm^{-1}}$ threshold for the homogeneous fields in Selhausen (a) and Braccagni (b), in relation to the standard deviation of SIF_{760} at field scale ($\sigma_{SIF_{760}^{fields}}$).

(a)

(b)

Figure 16: Number of sampling points needed to reach the $0.2\,\mathrm{mWm^{-2}sr^{-1}nm^{-1}}$ threshold for the FLEX pixels in Selhausen (a) and Braccagni (b), in relation to the standard deviation of SIF_{760} at FLEX pixel scale ($\sigma_{SIF_{760}^{FLEX}}$).
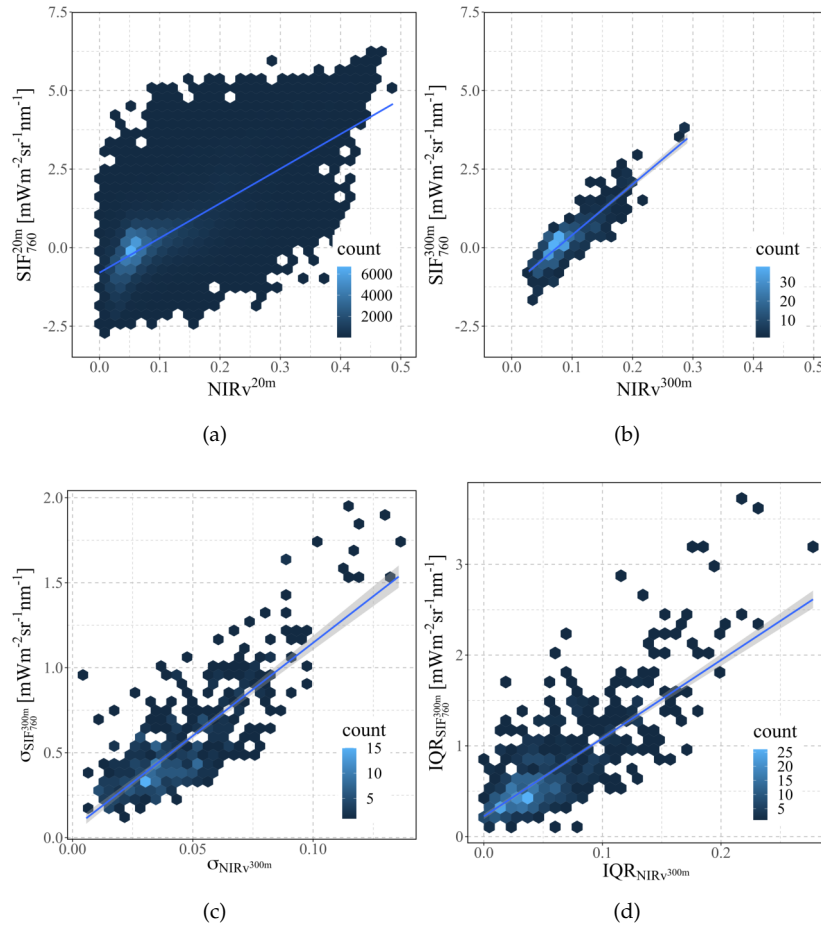
Figure 17: Relationship between SIF_{760} values and NIRv in the study area of Braccagni (Italy): a) SIF_{760} and NIRv values at $20\,\mathrm{m} \times 20\,\mathrm{m}$ spatial resolution; b) SIF_{760} and NIRv values at $300\,\mathrm{m} \times 300\,\mathrm{m}$ spatial resolution; c) standard deviation (*sigma*) of SIF_{760} and NIRv values at $300\,\mathrm{m} \times 300\,\mathrm{m}$ spatial resolution; d) interquartile range (IQR) of SIF_{760} and NIRv values at $300\,\mathrm{m} \times 300\,\mathrm{m}$ spatial resolution. Robust linear regression models are shown, cell colour is linked to data density.
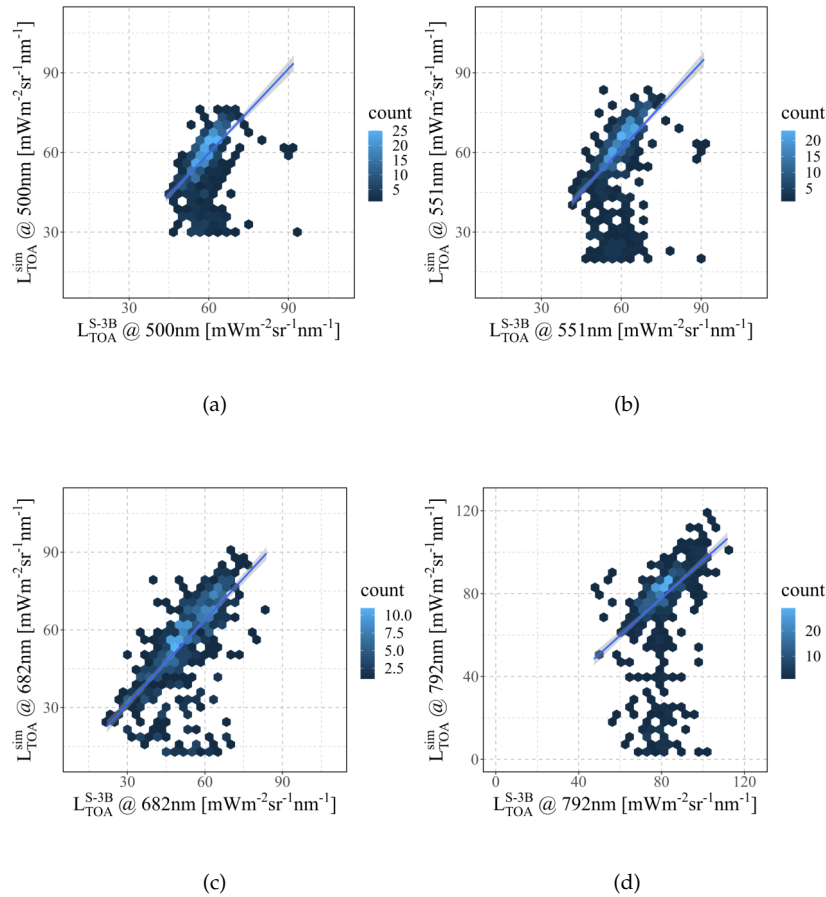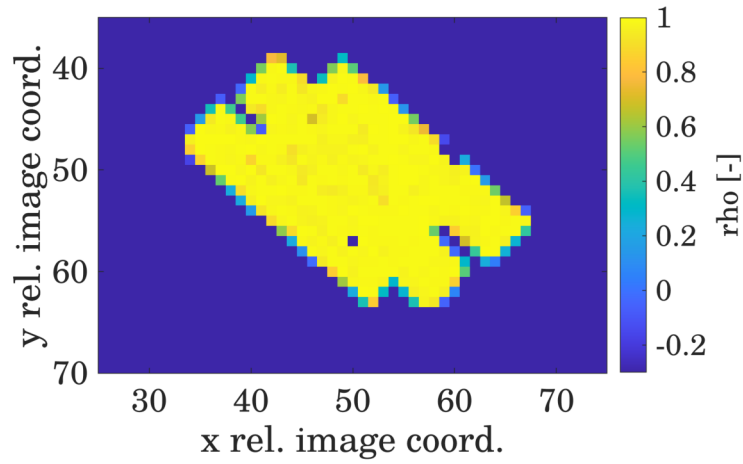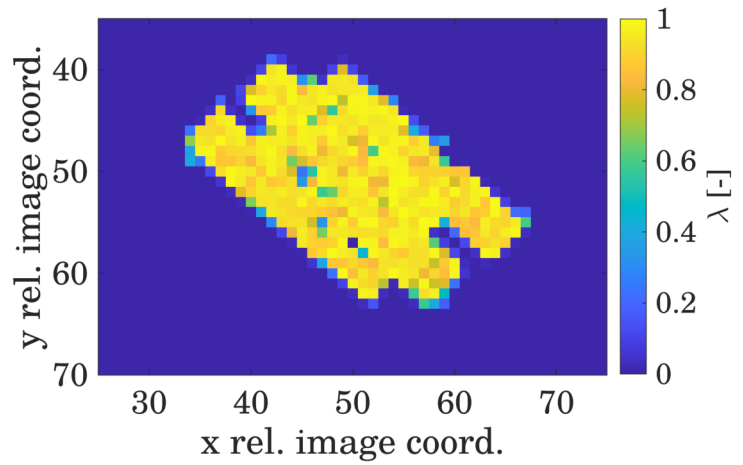
Figure 18: Scatterplot between the TOA radiance from S-3B (L_{TOA}^{S-3B}) and the TOA radiance simulated with MODTRAN and HyPlant surface reflectance (L_{TOA}^{sim}) for four spectral bands: a) 500 nm; b) 551 nm; c) 682 nm; d) 792 nm. The robust regression linear model fitted to the data is reported as well.

(a)

(b)

Figure 19: a) Pearson's correlation coefficient (rho) and b) lambda agreement index (λ) computed between the TOA radiance from S-3B (L_{TOA}^{S-3B}) and the TOA radiance simulated with MODTRAN and HyPlant surface reflectance (L_{TOA}^{sim}).
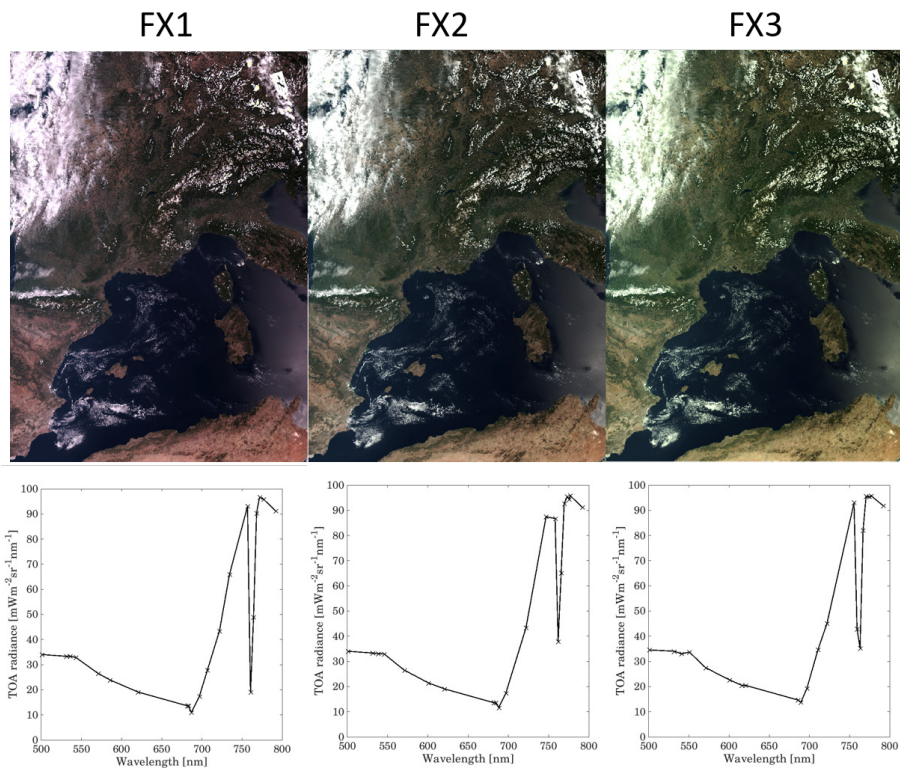
Figure 20: *Top:* Example of S-3B L-1b TOA radiance for the three spectral susbsets (FX1-3, "OLCI L1 - Tristimulus" synthesis). *Bottom:* corresponding spectra extracted from a vegetated pixel.
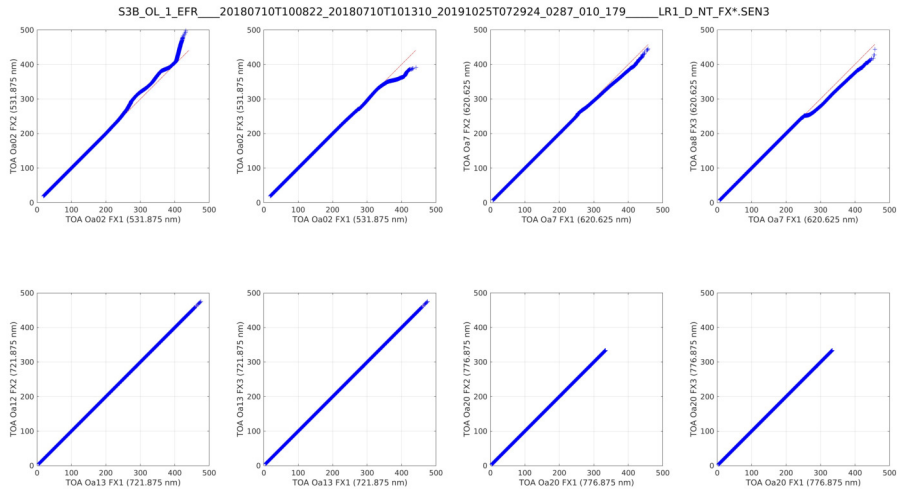
Figure 21: Q-Q plots of the bands common to the three spectral subsets (FX1-3) without quality flags filtering.
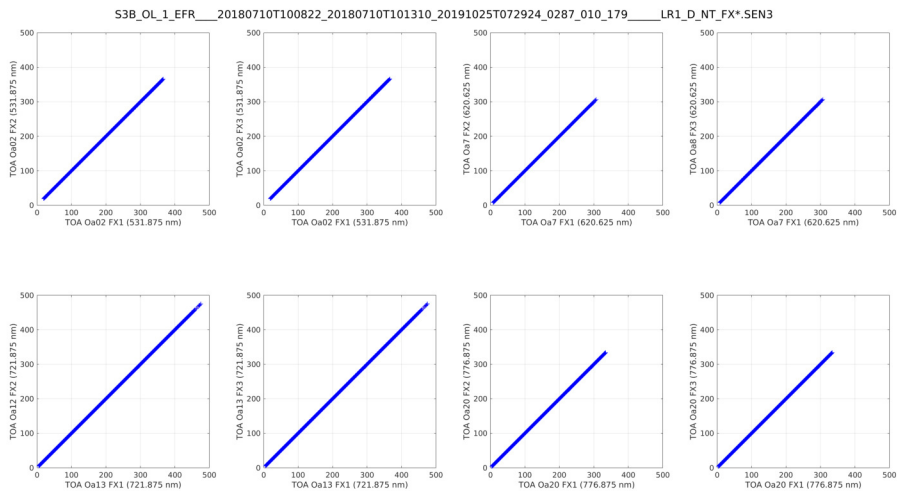

Figure 22: Q-Q plots of the bands common to the three spectral subsets (FX1-3) after removal of saturated pixels.
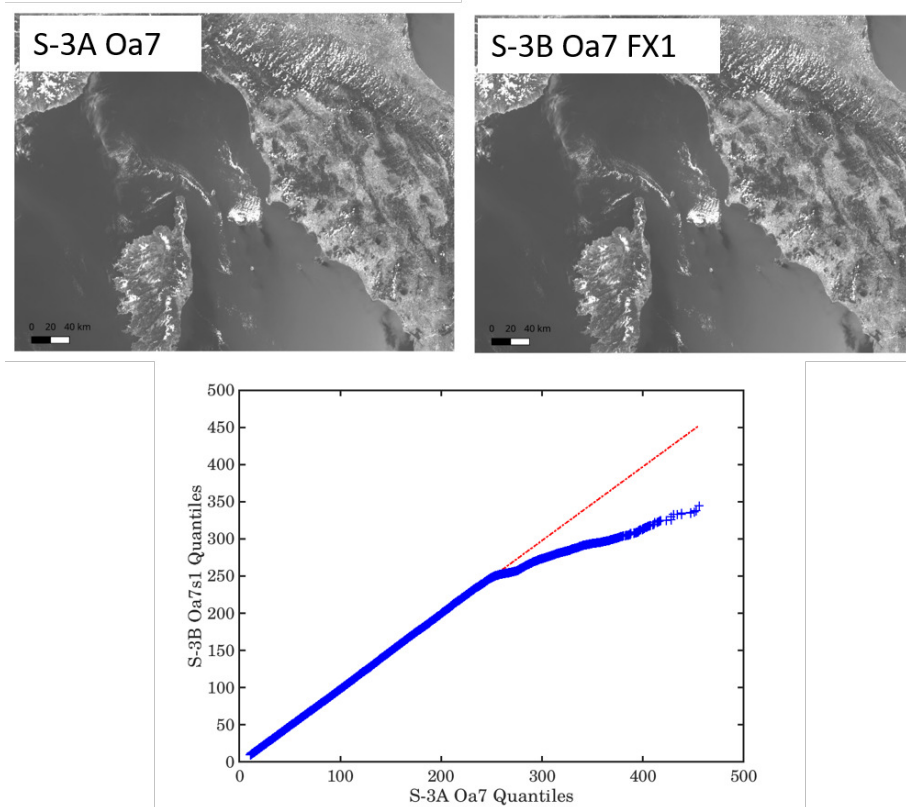
Figure 23: *Top:* Comparison of the L-1b S-3A OLCI Oa7 TOA values and the "FLEX mode" L-1b S-3B OLCI Oa7 TOA values taken from the FX1 spectral subset; *Bottom:* quantile-quantile (Q-Q) plot of the values extracted from the two products above.

Figure 24: Temporal trends of selected bands from the Sentinel-3A OLCI and the "FLEX mode" Sentinel-3B OLCI data over the La Crau site (43.558 85° N, 4.864 472° E). TOA reflectance values are averaged in a 3 pixels x 3 pixels (*i.e.*, ≈ 900 m × 900 m) region centred on the site.

4 Scientific outreach

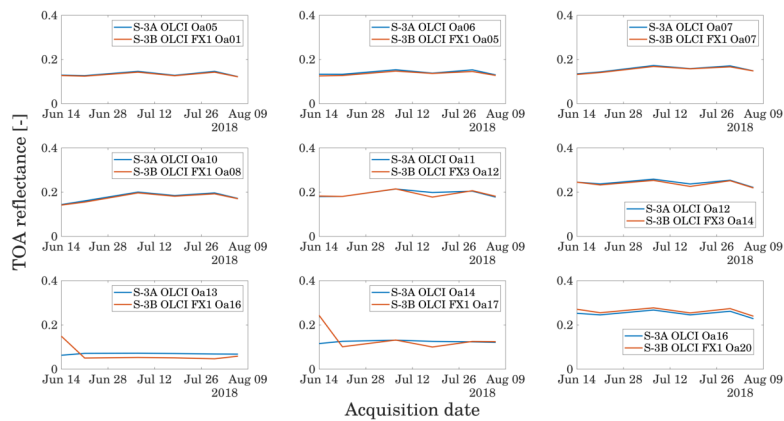## 4.1 Peer-reviewed publications

- Biriukova, K., Celesti, M. *et al.* (2020) Effects of varying solar-view geometry and canopy structure on solar-induced chlorophyll fluorescence and PRI. *ISPRS Journal of Photogrammetry and Remote Sensing*. Corresponding author, `https://doi.org/10.1016/j.jag.2020.102069`

- Hao, D., [. . .] Celesti, M. *et al.* (In press) Practical approaches for normalizing directional solar-induced fluorescence to a standard viewing geometry. *Remote Sensing of Environment*

- Tagliabue, G., Panigada, C., Celesti, M. *et al.* (2020). Sun–induced fluorescence heterogeneity as a measure of functional diversity. *Remote Sensing of Environment*, 247, 111934. `https://doi.org/10.1016/j.rse.2020.111934`

- Celesti, M. *et al.* (under review) Sentinel-3B OLCI in "FLEX mode" during the tandem phase: a new opportunity for fluorescence retrieval from space. Submitted to *Scientific Data*

- Celesti, M. *et al.* (in preparation) A data driven approach to define proximal sensing protocols towards the validation of medium resolution SIF products. To be submitted to *ISPRS Journal of Photogrammetry and Remote Sensing*

- Celesti, M. *et al.* (in preparation) Exploring continuous time series of vegetation hyperspectral reflectance and solar-induced fluorescence through radiative transfer model inversion. To be submitted to *Remote Sensing*

4.2 Projects

Several projects were linked with MULTI-FLEX and will benefit from the outcome of this project, both in terms of data and methodology. In particular:

- "Optical synergies for spatiotemporal SENsing of Scalable ECOphysiological traits" (SENSECO) COST Action CA17134;

- ESA "ATMO-FLEX" and "ATMO-FLEX CCN" projects;

- ESA "FLEXSense" project;

- ESA "SF TAPE" project (Lena Janicke, Ph.D. student at the Free University of Berlin);

- "Algorithms development for chlorophyll fluorescence signal evaluation generated from inland waters and terrestrial vegetation using hyperspectral remote sensing and radiative transfer models" (Ilaria Cesana, Ph.D. student at the University of Milano-Bicocca)

4.3 Conferences and workshops

- Celesti, M. (2020) Sentinel-3B OLCI in "FLEX mode" during the tandem phase: a novel dataset towards the future synergistic FLEX/S-3 mission. *To be presented at the Sentinel-3 Validation Team meeting, 15-17 December 2020, online.*

- Celesti, M. (2020) Exploring continuous time series of vegetation hyperspectral reflectance and solar-induced fluorescence through radiative transfer model inversion. *Presented at the EGU 2020 general assembly, 4-8 May 2020, online.*

- Celesti, M. *et al.* (2019) Exploring the Physiological Information of Solar-Induced Chlorophyll Fluorescence Through Radiative Transfer Model Inversion: a Multi-Scale Approach From Ground to Airborne Data. *ESA Living Planet Symposium, 13-17 May 2019, Milan, Italy;*

- Celesti, M. *et al.* (2019) Sentinel-3B OLCI in "FLEX mode" during the tandem phase: a new opportunity for fluorescence retrieval from space. *ESA Living Planet Symposium, 13-17 May 2019, Milan, Italy;*

- Celesti, M. *et al.* (2019) Exploring continuous time series of vegetation hyperspectral reflectance and solar-induced fluorescence through radiative transfer model inversion. *AGU Fall meeting, 9-13 December 2019, San Francisco, USA;*

- Celesti, M. (2019) "MULTI-FLEX" Living Planet Fellowship: Concurrent retrieval of Solar-induced fluorescence and plant traits from multi-scale hyperspectral data. *Presented at the ESA FLEX Mission Advisory Group meeting, 25 June 2019, ESA-ESTEC, The Netherlands;*

- Celesti, M. (2019) Solar-induced fluorescence (<) scaling: an issue with many contributors. *Presented at the SENSECO COST action WG1 workshop, 26 September 2019, Budapest, Hungary;*

- Celesti, M. (2019) Satellite based imagery from the 2018 campaign – overview on the S-2 and S-3 data and the processing of the S-3B reprogrammed data. *Presented at the ESA ATMO-FLEX/FLEXSense progress meeting, 14-17 September 2019, ESA-ESRIN, Italy;*

- Hueni, A. and Celesti, M. (2019) FLUOSPECCHIO: a spectral information system in support of the FLEX mission calibration/validation activities. *Presented at the SENSECO COST action WG1-WG2-WG3-WG4 joint workshop, 28-30 October 2019, Lanzarote, Spain;*

- Celesti, M. (2019) Overview of the S-3B OLCI data reprogrammed in "FLEX mode". *Presented at the Sentinel-3 Mission Performance Group meeting, 5 November 2019.*

References

Badgley, G., L. D. L. Anderegg, J. A. Berry, and C. B. Field (Nov. 2019). "Terrestrial gross primary production: Using NIR $_V$ to scale from site to globe". In: *Global Change Biology* 25.11, pages 3731–3740. DOI: `10.1111/gcb.14729` (cited on page 15).

Celesti, M., C. van der Tol, S. Cogliati, C. Panigada, P. Yang, F. Pinto, U. Rascher, F. Miglietta, R. Colombo, and M. Rossini (Sept. 2018). "Exploring the physiological information of Sun-induced chlorophyll fluorescence through radiative transfer model inversion". In: *Remote Sensing of Environment* 215, pages 97–108. DOI: `10.1016/j.rse.2018.05.013` (cited on pages 8, 9).

Cogliati, S., R. Colombo, M. Celesti, G. Tagliabue, U. Rascher, A. Schickling, P. Rademske, L. Alonso, N. Sabater, D. Schuettemeyer, D. Schuettemeyer, M. Drusch, D. Schuettemeyer, and M. Drusch (2018). "Red and far-red fluorescence emission retrieval from airborne high-resolution spectra collected by the hyplant-fluo sensor". In: *International Geoscience and Remote Sensing Symposium (IGARSS)* 2018-July, pages 3935–3938. DOI: `10.1109/IGARSS.2018.8517758` (cited on page 15).

Cogliati, S., W. Verhoef, S. Kraft, N. Sabater, L. Alonso, J. Vicent, J. Moreno, M. Drusch, and R. Colombo (2015). "Retrieval of sun-induced fluorescence using advanced spectral fitting methods". In: *Remote Sensing of Environment* 169, pages 344–357. DOI: `10.1016/j.rse.2015.08.022` (cited on pages 8, 10, 17).

Cogliati, S., M. Celesti, I. Cesana, F. Miglietta, L. Genesio, T. Julitta, D. Schuettemeyer, M. Drusch, U. Rascher, P. Jurado, P. Jurado, R. Colombo, P. Jurado, and R. Colombo (Aug. 2019). "A Spectral Fitting Algorithm to Retrieve the Fluorescence Spectrum from Canopy Radiance". In: *Remote Sensing* 11.16, page 1840. DOI: `10.3390/rs11161840` (cited on pages 8, 10).

Drusch, M., J. Moreno, U. D. Bello, R. Franco, Y. Goulas, A. Huth, S. Kraft, E. M. Middleton, F. Miglietta, G. Mohammed, L. Nedbal, U. Rascher, D. Schüttemeyer, and W. Verhoef (2017). "The FLuorescence EXplorer Mission Concept—ESA's Earth Explorer 8". In: *IEEE TRANSACTIONS ON GEOSCIENCE AND REMOTE SENSING* 55.3, pages 1273–1284 (cited on page 3).

Duveiller, G., D. Fasbender, and M. Meroni (2016). "Revisiting the concept of a symmetric index of agreement for continuous datasets". In: *Scientific Reports* 6.1, page 19401. DOI: `10.1038/srep19401` (cited on page 18).

Franklin, J., J. M. Serra-Diaz, A. D. Syphard, and H. M. Regan (Apr. 2016). "Global change and terrestrial plant community dynamics". In: *Proceedings of the National Academy of Sciences* 113.14, pages 3725–3734. DOI: `10.1073/pnas.1519911113` (cited on page 2).

Julitta, T., L. A. Corp, M. Rossini, A. Burkart, S. Cogliati, N. Davies, M. Hom, A. M. Arthur, E. M. Middleton, U. Rascher, A. Schickling, and R. Colombo (Feb. 2016). "Comparison of sun-induced chlorophyll fluorescence estimates obtained from four portable field spectroradiometers". In: *Remote Sensing* 8.2, page 122. DOI: `10.3390/rs8020122` (cited on page 20).

Meroni, M., L. Busetto, R. Colombo, L. Guanter, J. Moreno, and W. Verhoef (Feb. 2010). "Performance of Spectral Fitting Methods for vegetation fluorescence quantification". In: *Remote Sensing of Environment* 114.2, pages 363–374. DOI: 10.1016/j.rse.2009.09.010 (cited on pages 8, 10).

Meroni, M. and R. Colombo (Aug. 2006). "Leaf level detection of solar induced chlorophyll fluorescence by means of a subnanometer resolution spectro-radiometer". In: *Remote Sensing of Environment* 103.4, pages 438–448. DOI: 10.1016/j.rse.2006.03.016 (cited on page 8).

Meroni, M., M. Rossini, L. Guanter, L. Alonso, U. Rascher, R. Colombo, and J. Moreno (Oct. 2009). "Remote sensing of solar-induced chlorophyll fluorescence: Review of methods and applications". In: *Remote Sensing of Environment* 113.10, pages 2037–2051. DOI: 10.1016/j.rse.2009.05.003 (cited on page 3).

Miao, G., K. Guan, A. E. Suyker, X. Yang, T. J. Arkebauer, E. A. Walter-Shea, H. Kimm, G. Y. Hmimina, J. A. Gamon, T. E. Franz, C. Frankenberg, J. A. Berry, and G. Wu (Feb. 2020). "Varying Contributions of Drivers to the Relationship Between Canopy Photosynthesis and Far-Red Sun-Induced Fluorescence for Two Maize Sites at Different Temporal Scales". In: *Journal of Geophysical Research: Biogeosciences* 125.2. DOI: 10.1029/2019JG005051 (cited on page 24).

Mohammed, G. H., R. Colombo, E. M. Middleton, U. Rascher, C. van der Tol, L. Nedbal, Y. Goulas, O. Pérez-Priego, A. Damm, M. Meroni, J. Joiner, S. Cogliati, W. Verhoef, Z. Malenovský, J. P. Gastellu-Etchegorry, J. R. Miller, L. Guanter, J. Moreno, I. Moya, J. A. Berry, C. Frankenberg, and P. J. Zarco-Tejada (2019). "Remote sensing of solar-induced chlorophyll fluorescence (SIF) in vegetation: 50 years of progress". In: *Remote Sensing of Environment* 231. DOI: 10.1016/j.rse.2019.04.030 (cited on page 3).

Monson, R. and D. Baldocchi (2013). *Terrestrial biosphere-atmosphere fluxes*, pages 1–495. DOI: 10.1017/CBO9781139629218 (cited on page 2).

Porcar-Castell, A., E. Tyystjärvi, J. Atherton, C. Van Der Tol, J. Flexas, E. E. Pfündel, J. Moreno, C. Frankenberg, and J. A. Berry (Aug. 2014). "Linking chlorophyll a fluorescence to photosynthesis for remote sensing applications: Mechanisms and challenges". In: *Journal of Experimental Botany* 65.15, pages 4065–4095. DOI: 10.1093/jxb/eru191 (cited on page 3).

Siegmann, B., L. Alonso, M. Celesti, S. Cogliati, R. Colombo, A. Damm, S. Douglas, L. Guanter, J. Hanuš, K. Kataja, F. Zemek, and U. Rascher (2019). "The high-performance airborne imaging spectrometer HyPlant-from raw images to top-of-canopy reflectance and fluorescence products: Introduction of an automatized processing chain". In: *Remote Sensing* 11.23. DOI: 10.3390/rs11232760 (cited on page 15).

Tagliabue, G., C. Panigada, M. Celesti, S. Cogliati, R. Colombo, M. Migliavacca, U. Rascher, D. Rocchini, D. Schüttemeyer, and M. Rossini (2020). "Sun–induced fluorescence heterogeneity as a measure of functional diversity". In: *Remote Sensing of Environment* 247.May, page 111934. DOI: 10.1016/j.rse.2020.111934 (cited on page 15).

Tol, C. van der, W. Verhoef, J. Timmermans, A. Verhoef, and Z. Su (2009). "An integrated model of soil-canopy spectral radiances, photosynthesis, fluorescence, temperature and energy balance". English. In: *Biogeosciences* 6.12, pages 3109–3129. DOI: 10.5194/bg-6-3109-2009 (cited on page 8).

Tucker, C. J. (May 1979). "Red and photographic infrared linear combinations for monitoring vegetation". In: *Remote Sensing of Environment* 8.2, pages 127–150. DOI: 10.1016/0034-4257(79)90013-0 (cited on page 15).

Verhoef, W., C. V. D. Tol, E. M. Middleton, C. Van der Tol, and E. M. Middleton (2014). "Vegetation Canopy Fluorescence and Reflectance Retrieval By Model Inversion Using Optimization". In: *5th International Workshop on Remote Sensing of Vegetation Fluorescence* 1, pages 759–770 (cited on page 17).